

Experimental and Numerical Investigation of Vortex Shedding of a Representative UCAV Configuration for Vortex Flow Control

Terence A. Ghee^{*}, Doug R. Hall[†]

NAVAIR, Code 4321

Bldg. 2187, Suite 1320B

Patuxent River, MD 20670-1906

USA

ABSTRACT

A 4% Uninhabited Combat Air Vehicle (UCAV) has been extensively tested at low speeds in a wind tunnel to investigate using vortex flow control to control vehicle attitude. The program is the initial step to utilize experimental and computational techniques to understand the flowfield environment on a representative low-observable air vehicle and use that understanding to apply an efficient vortex flow control apparatus. Gross flow field characteristics were identified using flow visualization and the approximate vortex location was determined for a number of angles-of-attack for a tunnel dynamic pressure of 26.74 psf. From this study, the model was instrumented with pressure transducers at appropriate locations on the wing and unsteady data was acquired for a number of angles-of-attack and tunnel dynamic pressures. A six-component internal balance was then installed to measure aerodynamic forces and moments. Limited steady electronically scanned pressure data were acquired. Computational fluid dynamic (CFD) analysis was conducted on the model geometry to compare with the results from the wind tunnel study. The results show two vortex structures: a weak apex vortex and a stronger wing vortex. Wing vortex frequency exhibits a broad-banded dominant frequency of approximately 10 Strouhal number. Maximum suction pressure was seen to move forward on the wing leading edge as the wing vortex moved inboard with increasing angle-of-attack. The CFD results adequately predicted the force and moment data. However, the CFD comparison to the unsteady pressure data was not stellar: CFD frequently failed to predict the mean pressure coefficient and the frequency content of the signal.

NOMENCLATURE

b	span, 2.160 ft	Re	Reynolds number, $(\rho_{\infty} V_{\infty} MAC)/\mu_{\infty}$, 0.73E6
C	coherence	RMS	root mean square
C_p	pressure coefficient, $p - p_{\infty}/q_{\infty}$	std	standard deviation
C_R	root chord, 1.280 ft	Se	transducer sensitivity, volt/psi
f	frequency, Hz	S	wing area, 1.210 ft ²
G	amplifier gain	St	Strouhal number, $(b f)/V_{\infty}$
I_{raw}	raw integer value (digital)	t	time, sec
MAC	mean aerodynamic chord, 0.765 ft	V	excitation voltage, 10 volt
M_{∞}	freestream Mach number, V_{∞}/a_{∞} , 0.13	V_{∞}	tunnel freestream velocity, 150 ft/s
P	pressure, psi	α	geometric angle of attack, degree
P_{Ref}	reference pressure, psi	μ_{∞}	viscosity, 3.7373E-7, slug/(ft sec)
PSD	power spectral density	τ	non-dimensional time, $(t a_{\infty})/MAC$
q_{∞}	tunnel dynamic pressure, 26.74 psf		

INTRODUCTION

On air vehicles with swept wings, leading edge vortices are created at off-design conditions, Ref. 1. The leading edge vortex generally has a beneficial effect in the form of increased lift at higher angles-of-attack. By

^{*} Aerospace Engineer, ph: 301 342 8536 FAX: 301 342 8588, gheeta@navair.navy.mil

[†] Aerospace Engineer, ph: 301 342 8534, FAX: 301 342 8588, halldr@navair.navy.mil

Report Documentation Page				Form Approved OMB No. 0704-0188	
Public reporting burden for the collection of information is estimated to average 1 hour per response, including the time for reviewing instructions, searching existing data sources, gathering and maintaining the data needed, and completing and reviewing the collection of information. Send comments regarding this burden estimate or any other aspect of this collection of information, including suggestions for reducing this burden, to Washington Headquarters Services, Directorate for Information Operations and Reports, 1215 Jefferson Davis Highway, Suite 1204, Arlington VA 22202-4302. Respondents should be aware that notwithstanding any other provision of law, no person shall be subject to a penalty for failing to comply with a collection of information if it does not display a currently valid OMB control number.					
1. REPORT DATE 00 MAR 2003		2. REPORT TYPE N/A		3. DATES COVERED -	
4. TITLE AND SUBTITLE Experimental and Numerical Investigation of Vortex Shedding of a Representative UCAV Configuration for Vortex Flow Control				5a. CONTRACT NUMBER	
				5b. GRANT NUMBER	
				5c. PROGRAM ELEMENT NUMBER	
6. AUTHOR(S)				5d. PROJECT NUMBER	
				5e. TASK NUMBER	
				5f. WORK UNIT NUMBER	
7. PERFORMING ORGANIZATION NAME(S) AND ADDRESS(ES) NATO Research and Technology Organisation BP 25, 7 Rue Ancelle, F-92201 Neuilly-Sue-Seine Cedex, France				8. PERFORMING ORGANIZATION REPORT NUMBER	
9. SPONSORING/MONITORING AGENCY NAME(S) AND ADDRESS(ES)				10. SPONSOR/MONITOR'S ACRONYM(S)	
				11. SPONSOR/MONITOR'S REPORT NUMBER(S)	
12. DISTRIBUTION/AVAILABILITY STATEMENT Approved for public release, distribution unlimited					
13. SUPPLEMENTARY NOTES Also see: ADM001490, Presented at RTO Applied Vehicle Technology Panel (AVT) Symposium held inLeon, Norway on 7-11 May 2001, The original document contains color images.					
14. ABSTRACT					
15. SUBJECT TERMS					
16. SECURITY CLASSIFICATION OF:			17. LIMITATION OF ABSTRACT UU	18. NUMBER OF PAGES 18	19a. NAME OF RESPONSIBLE PERSON
a. REPORT unclassified	b. ABSTRACT unclassified	c. THIS PAGE unclassified			

controlling the location of the shed vortex or vortices, vehicle roll and pitch control may be possible. Uninhabited Combat Air Vehicles (UCAVs) that utilize stealth to avoid detection suffer a radar signature increase when control surfaces are deflected. Thus, there is an advantage to be gained by limiting flap deflection by utilizing vortex flow control to change vehicle attitude. However, a thorough understanding of the vehicle flowfield is needed to best mate a flow control device to the vehicle. In view of this, an experimental and numerical investigation was conducted on a representative UCAV configuration to define the flowfield and investigate methods to control vortex location and, ultimately, vehicle attitude. The test program was developed in three phases: 1) vortex location identification using laser light sheet flow visualization and fluorescent oil applied to the model surface, 2) vortex quantification through surface and off-body measurements, and 3) vortex manipulation utilizing a flow control device. This paper reports the results of the first two phases of the program.

EXPERIMENTAL SETUP

The tests were conducted in the Naval Aerodynamic Test Facility (NATF) as part of the Naval Air Warfare Center In-House Laboratory Independent Research (ILIR) program. The NATF is a four-foot by four-foot closed test section, open-return wind tunnel. The facility incorporates a 200 horsepower motor that drives a variable pitch fan and delivers a maximum velocity of 205 ft/s. In addition, the facility has honeycomb and three sets of flow conditioning screens that minimize freestream turbulence intensity to approximately 0.15% and freestream velocity differences of 1%. Fig. 1 shows the 4% UCAV model in the NATF.

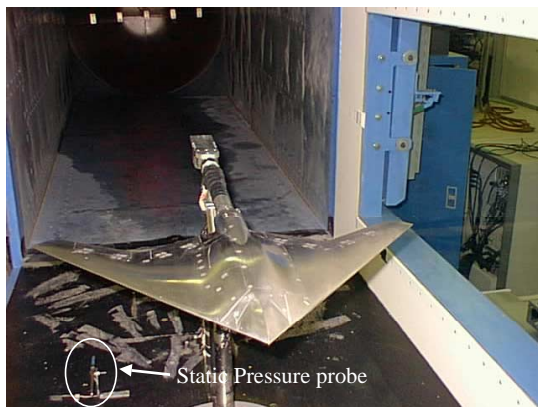


Fig. 1 – 4% UCAV in NATF

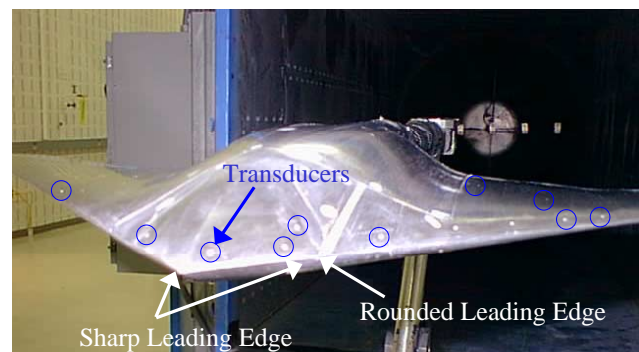


Fig. 2 - 4% UCAV Leading Edge

A 4% UCAV model with 47-degree leading edge was used as a representative configuration. The model was fabricated of stainless steel for the US Air Force Research Laboratory and tested previously to assess aerodynamic performance at high subsonic and transonic speeds, Ref. 2. The leading edge of the cranked-delta-wing vehicle has a sharp chine at the nose that transitions to round in the vicinity of the wing/body juncture, see Fig. 2. All data reported herein was for the boundary layer transition free. Also visible in Fig. 2 and detailed in Fig. 3, are the 13 Kulite fast-response, 5-psi sealed-gauge, pressure transducers installed on the model. An inlet nose plug was installed for the majority of the testing to create a more simplified geometry without the added complexity of a flow-through duct. In addition, transducer signal/power cables could be run through the duct, thus avoiding expensive machining of the model. The nose/propulsion inlet plug also allows the testing of novel vortex flow control devices to be easily fabricated and evaluated when affixed to the plug.

A sting assembly attached to the facility pitch strut supported the model and the support system was constrained vertically; the model moved off-centerline with changing angle-of-attack. Angle-of-attack was measured at the model support system using an Allied Signal QA-2000 accelerometer. The model was set to 0.108 degrees in yaw to correct cross flow angularity.

The unsteady pressure data was acquired using a 32-channel, 14-bit DSP Technology, Inc. IMPAX unsteady data acquisition system connected to a personal computer. This system acquired the data simultaneously and thus the data was coincident.

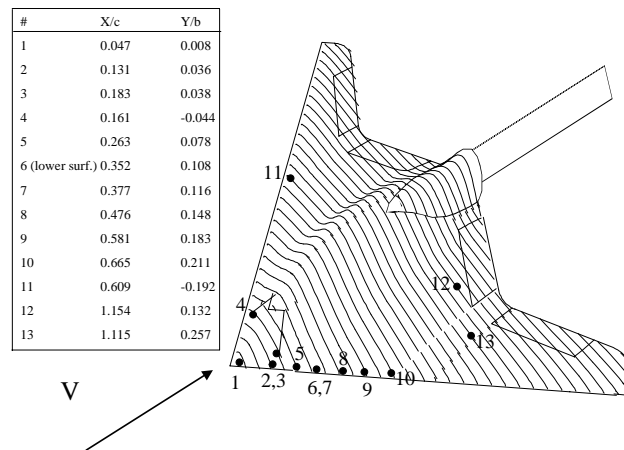
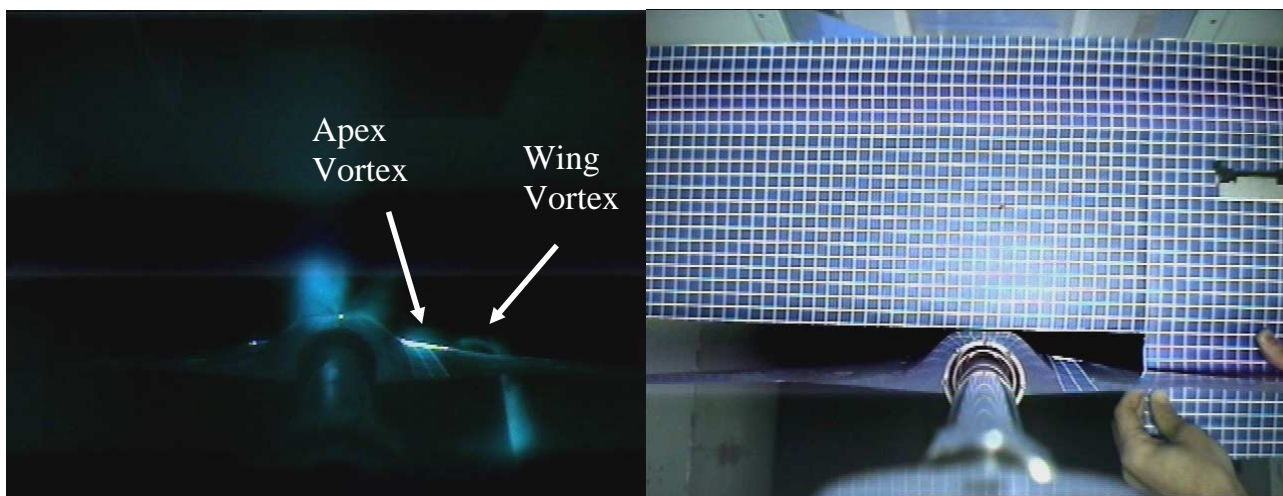


Fig. 3 – Transducer Location



a) Video data, view looking upstream.

b) Reference grid video, used to quantify vortex location

Fig. 4 – Vortex Location Using Laser Light Sheet, $x/MAC = 0.735$

PROCEDURE AND DATA REDUCTION

PHASE 1

A flow visualization study was conducted utilizing laser light sheet and injected vaporized propylene glycol to seed the flow. A miniature camera was mounted to the support system strut and orthogonal to the light sheet. To quantify the location of the vortices in space, video data was acquired at a tunnel dynamic pressure of 26.74 psf and at angles-of-attack from 6 to 14 degrees in increments of 2 degrees. After tunnel shutdown, a reference grid was placed in the plane of the light sheet. See Fig. 4 for an example of video data and the reference grid. Using a known reference location on the grid, digital image processing techniques, and an in-house developed digitizing code (DigitVB), the vortex locations were determined. In addition, fluorescent oil flow visualization studies were conducted at an angle-of-attack of 10 degrees and for wind tunnel velocities of 75 ft/s, 100 ft/s, 125 ft/s, and 150 ft/s, see Fig. 5. Note: Fig. 5 has been digitally enhanced for clarity. Both of these studies were performed utilizing a dummy balance. This allowed angular deformations to be minimized. The results from this phase were used to guide transducer placement on the model.

PHASE 2

The unsteady pressure tests reported herein were conducted at a constant tunnel velocity of 150 ft/s ($q_\infty = 26.74$ psf and Reynolds number of 0.73 million based on MAC). Model incidence was varied from 0 degrees to 18 degrees in increments of 1 degree for the unsteady pressure portion of the testing. Thirty seconds of wind-off-

zero data were acquired previous to tunnel start up. The tunnel was driven to 150 ft/s and after test conditions steadied, unsteady pressure data were acquired. Unsteady pressures were sampled at 10,000 samples/second for 30 seconds. A Butterworth 8-pole filter provided a low-pass cut off frequency of 2,000 Hz. Following tunnel shutdown, wind-off-zero data were acquired for comparison to the pre-test wind-off-zero data. The data was analyzed to determine the time-history and PSD characteristics. The large size of the data array (307200

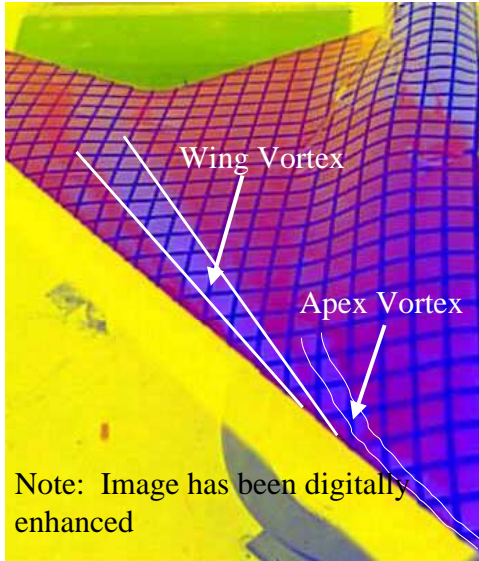


Fig. 5 – Oil Flow at $\alpha = 10$ Degrees

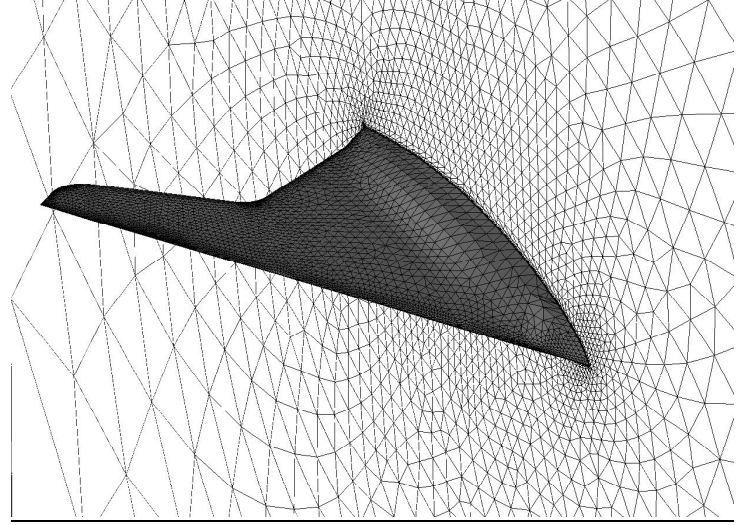


Fig. 6 – CFD Grid

samples per transducer per run) necessitated the data be analyzed on a high performance computer system. Matlab software was used to determine the pressure time history and pressure power spectral density (PSD) using an SGI Octane computer workstation. A Mensor digital pressure gauge was used to measure the reference barometric pressure needed to obtain the measured absolute pressure from the sealed gauge transducers. Pressure coefficient data were then determined by the following:

$$C_p = \frac{(P_{\text{measured}} - P_{\text{wind-off zero}}) - P_{\infty}}{(q_{\infty})}$$

The coherent acoustic noise present in the freestream data was removed from the pressure measurements by using an unsteady static pressure probe located on the tunnel floor, see Fig. 1. The coherence was a function of the power spectrum of the freestream noise and the power spectrum of the data at an arbitrary angle-of-attack and the cross spectrum of the freestream noise and the data at the arbitrary angle-of-attack, see Refs. 3 and 4. Thus, the coherence was found by:

$$C = \frac{(\text{PSD}_{\text{Ref., meas}})^2}{(\text{PSD}_{\text{Ref., Ref.}} * (\text{PSD}_{\text{meas, meas}}))}$$

The PSD of the measured data was then corrected:

$$\text{PSD}_{\text{meas}} = (1 - C) * \text{PSD}_{\text{meas, uncorrected}} \quad (\text{RMS}^2)$$

The algorithm to determine the PSD was based on the method by Welch, Ref. 5. The data were segmented into windows to allow thirty averages and corresponded to a frequency resolution of 1 Hz. No data overlapping was employed and a Hanning filter was used with a window length the same size as the data segments. The mean was

eliminated from the PSD and coherence calculations and a 95% confidence criterion was used to gage the PSD assessment.

Table 1 - Balance Uncertainty								
% FS - Calibration Plus Proof Loads								
	NF	AF	PM	RM	YM	SF	C_L @ 46 psf, $\alpha=0$	C_D @ 46 psf, $\alpha=0$
Maximum	0.12	0.81	0.14	0.22	0.16	0.07	0.007050253	0.004753289
Minimum	-0.07	-0.3	-0.12	-0.32	-0.2	-0.07		
FS Load	300 lb	30 lb	1,000 in-lb	150 in-lb	500 in-lb	200 lb		

Reported force and moment testing was accomplished at a tunnel dynamic pressure of 46.59 psf. This higher tunnel dynamic pressure allowed a higher loading on the balance and decreased coefficient measurement uncertainty. A Modern Machine UT-37BN six-component, sting-mounted balance replaced the dummy balance used in the previous studies. Table 1 provides details of the maximum full-scale loads and error report. The balance had been calibrated immediately before testing and first and second order interaction corrections were utilized. Limited electronically scanned pressure (ESP) data was obtained. This provided some wing pressures and quantified model base and cavity pressure. However, the force and moment data shown in this paper are uncorrected for the effect of the wind tunnel walls.

The CFD calculations were performed using the COBALT code, a time-accurate, unstructured Navier-Stokes solver, see Refs. 6 and 7. Cobalt solves the Navier-Stokes equations using a Riemann method. Implicit solutions are obtained on unstructured, cell centered, finite volume cells. The cell type is arbitrary. The volume grid consists of one zone that is subdivided for parallel processing. The grid model utilized a symmetry plane for the model and consisted of 381,000 cells, see Fig. 6. The solution was obtained at time step of 1/40,000 second. A Spalart-Allmaras turbulence model was employed. Full-scale Reynolds number at 150 Ft/s were calculated in a free-air case. Also, the effects of the aerodynamic distortion due to the wind tunnel sting were not accounted for in the CFD model.

ERROR ANALYSIS

An uncertainty estimate of the data was undertaken to gauge the accuracy of the test results. The unsteady pressure measurement accuracy was dictated by the quoted instrumentation repeatability of 0.1%. The effect of the accuracy of the A/D system and power supply was evaluated and found to be negligible on the data accuracy. (However, these uncertainties were incorporated in the error analysis.) The tunnel velocity varied in the test section by approximately 1% and fluctuated by approximately 0.75% at the tested tunnel velocity. Using a method outlined in Ref. 8, the uncertainty in pressure coefficient was estimated to be 0.027. The highest and lowest resolvable frequencies were 2000 Hz and 0.03 Hz, respectively. These values were based on the use of a low-pass filter and dwell time. The Nyquist criteria would dictate the highest frequency of 4,267 Hz. The frequency that could be resolved in the PSD was approximately 1Hz. Table 1 provides estimates of the error associated with the balance data at a tunnel dynamic pressure of 46.59 psf.

RESULTS

To gain an understanding of the various flow-states on the UCAV, lift coefficient versus angle-of-attack and drag coefficient versus lift coefficient squared were evaluated for a tunnel dynamic pressure of 46.59 psf, see Figs. 7 and 8. In Fig. 7, the theoretical attached flow lift coefficient is given by:

$$C_L = C_{Lp} + K_p \sin \alpha \cos^2 \alpha$$

where C_{Lp} is the lift coefficient at $\alpha = 0$ degrees and K_p is the lift curve slope at $\alpha = 0$ degrees, Ref. 9. A lift curve slope break is seen to occur at approximately $\alpha = 2$ degrees (filled circle symbol) and corresponds to a

transition from attached to leading edge separated flow. Also plotted on Fig. 7 is the lift coefficient at $\alpha = 12$ degrees obtained by the CFD analysis.

Due to the poor balance resolution at low values of drag coefficient, it is difficult to quantify the boundary from attached to separated flow in Fig. 8. However, Fig. 8 does provide insight into other flow-states existing on the wing. Theoretical estimates for the data, based upon linear least-squares fits, are shown within the respective mid-alpha and high-alpha ranges. Changes in flow-state manifest themselves as changes in a linear slope of the plot. At approximately $C_L^2 = 0.25$ or an $\alpha = 7.5$ degrees, another lift curve slope break point was seen to occur (filled circle symbol) and was most likely due to the outboard panel of the wing separating. Another lift curve slope break point was seen to occur at $C_L^2 = 0.51$ or an $\alpha = 13$ degrees, again tagged by a filled circle symbol. The drag rise after $C_L^2 = 0.51$ is more quadratic in nature and implies a change in the character of the separated flow: the bursting of the wing vortex.

Drag force and pitching moment coefficient were plotted against lift coefficient and are shown in Figs. 9 and 10. The lift curve slope break points observed previously are plotted on these figures as filled circle symbols. Again, data from the CFD analysis is plotted for comparison. The relative insensitivity of the axial force balance beam caused significant scatter near C_{Dmin} . The pitching moment was seen to exhibit a slight nose up moment after the transition from attached to separated flow. A larger nose up pitching moment was realized after the second lift curve slope break point due to the outer wing panel separating. An increasing nose down moment due to wing vortex bursting was realized after the third lift curve slope break point.

From both CFD and Phase 1 experiments, two distinct vortex systems were found: one vortex emanating from the nose of the vehicle and a second vortex issuing from the wing leading edge, see Fig. 11. CFD analyses showed good agreement in the basic flow structure. The wing vortex was found to emanate at the transition from a sharp to rounded leading edge. Laser light sheet images were analyzed and the vortex location in space was quantified for an angle-of-attack of 10 degrees, see Fig. 12. Using fluorescent oil flow visualization, the wing vortex was found to emanate from the leading edge at an approximate location of $x/MAC=0.279$ and $y/b/2=0.184$. Also plotted on Fig. 12 are the transducer locations for the starboard side of the wing. The wing vortex appeared to burst between $x/MAC = 0.9$ to 1.0 for an $\alpha = 14$ degrees at a tunnel dynamic pressure of 26.74 psf. (Analyzing the vortex location for $\alpha = 14$ degrees, the wing vortex was seen to move noticeably inboard compared to the other angles-of-attack data.) For an $\alpha = 12$ degrees at a tunnel dynamic pressure of 26.74 psf, vortex burst appeared to occur closer to $x/MAC = 1.2$.

The results from the flow visualization studies were used to guide transducer placement; see Fig. 3 for transducer location. Unsteady pressure data were analyzed and plotted as a mean and standard deviation of the pressure coefficient versus angle-of-attack, see Figs. 13 and 14. Note: all pressure data uses uncorrected angle-of-attack and dynamic pressure. The mean pressure coefficient is an indication of the approximate vortex location along the leading edge. As angle-of-attack increases, the vortex was seen to move more inboard as evidenced in Fig. 13 by an increase in suction pressure toward the apex as the angle-of-attack increases (i.e., the maximum suction pressure for a given transducer location occurs at a lower angle-of-attack for increasing x/MAC). The flowfield appears to be slightly asymmetric as evidenced by Transducers 10 and 11 having different pressure characteristics.

The standard deviation of the pressure coefficient was a measure of the flow unsteadiness, see Fig. 14. The maximum standard deviation was seen to occur at a higher angle-of-attack than the maximum suction peak. Also note that Transducer 4 experienced a rapid rise in standard deviation at higher angles-of-attack. The location of Transducer 4 was in a region where, due to geometric blending of the body, nose, and wing, separated flow was possible.

PSD plots for Transducer 8 as a series of increasing angle-of-attack are presented in Fig. 15. This location was chosen because it generally was the first to exhibit a defined vortex frequency spectrum. At an angle-of-attack of 8 degrees, the only detectable frequency spikes were due to the wind tunnel fan. At this angle-of-attack, this

location was found to have no defined vortex frequency spectrum. This figure is typical for transducers located nearer the apex and most transducers at low to moderate angles-of-attack. As the angle-of-attack is increased, a broad frequency spike develops at this transducer location. The maximum Strouhal number of the spectrum varies as shown in Table 2. The Strouhal number was generally found to be near 10 for most leading edge locations. However, these numbers were determined based on the inflection point of the broad band spike (e.g., Fig. 8) and are not to be thought of as distinct frequencies.

The corresponding pressure coefficient time histories for Transducer 8 are shown in Fig. 16. Non-dimensional time is plotted for the equivalent of 0.2 seconds. A low frequency pulse is seen at an angle-of-attack of 16 degrees. This pulse was seen at the same angle-of-attack in Fig. 15 as a large spike at a Strouhal number of 0.5. The low frequency pulse also corresponds to the maximum standard deviation seen in Fig. 14 for this transducer.

Plots of PSD for Transducer 2 (apex of vehicle) and 12 (furthest aft) are plotted in Figs. 17 and 18. As mentioned previously, little frequency content was noted for transducers located near the nose and at low to moderate angle-of-attack, see Fig 17. Increasing angle-of-attack to 14 to 18 degrees, Transducer 2 measured a broad band signal indicative of a separated flowfield.

In Fig. 18, Transducer 12 exhibited a more defined spectrum at an angle-of-attack of 10 degrees. At this location and angle-of-attack the vortex had not burst. However, increasing angle-of-attack to 14 degrees, a broad band spectrum was seen. From flow visualization results discussed previously, the wing vortex had burst at this location and angle-of-attack. Increasing angle-of-attack further to 18 degrees, a curious spike was noted. At this time, the explanation for this is being studied.

A first attempt comparison of experiment unsteady pressure to CFD predictions are shown in Figs. 19 and 20. The comparison of PSD signal content shows poor comparison of CFD to the experimental data, see Fig. 19. Note: the vertical scale is not constant across the family of plots. The data was analyzed using Welch's method and utilized the same sample size, sample rate, and blocks (or windows) of data. Unfortunately, the CFD prediction was for a full-scale Reynolds number. The effect of Reynolds number on the flow would be to change the location and strength of the vortex, Ref. 10. In addition, the frequency content of the full-scale Reynolds number would be much lower. This raises a concern that the sample length (0.3 seconds) may not be of adequate length to resolve the frequency content.

As seen in Fig. 20 and Table 3, CFD poorly predicts the mean pressure coefficient and signal content (standard deviation).

Additional analysis must be performed before a fair assessment of CFD ability to predict the unsteady flowfield can be made. These include scaling the Reynolds number, increasing grid resolution in the vicinity of the vortex formation to insure adequate resolution of small-scale eddy structure off the prime separation, investigating time step adequacy, and using an improved turbulence model.

Initially, apex blowing was to be utilized to facilitate vortex flow control. This may be attempted but, given the fact of a weak apex vortex that is distinct from the wing vortex and little flow dynamic frequency content, repositioning the apex vortex through steady or pulsed blowing appears unlikely to affect the wing vortex. It may be possible to utilize tangential leading edge blowing on the nose plug to initiate the wing vortex and that may be an avenue to explore. Currently, the use of leading edge micro-vortex generators is being investigated and will be researched later this year. The cost to the low observable signature remains to be determined.

CONCLUSIONS

A comprehensive test program was accomplished to determine the flowfield characteristics of a representative UCAV configuration. The tests were conducted in the US Navy NATF wind tunnel at a tunnel dynamic pressure of 26.74 psf. The results show that the air vehicle has two flow structures: an apex and wing vortex. Of the two, the wing vortex appears to be much stronger. The apex vortex exhibited little dynamic frequency content while the wing vortex exhibited a broad band frequency with a Strouhal number of 10. Little interaction was noted

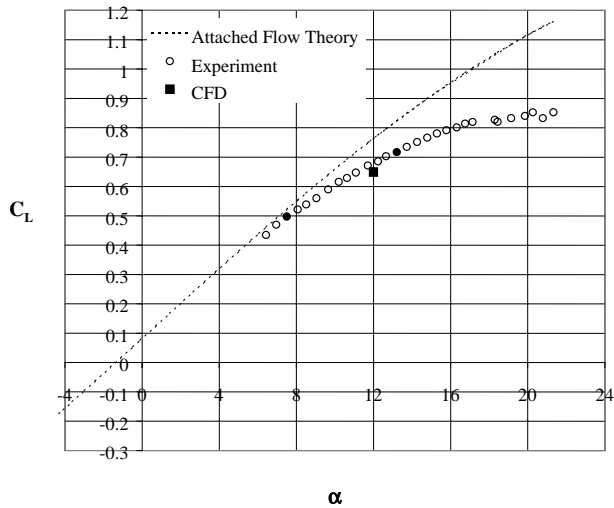
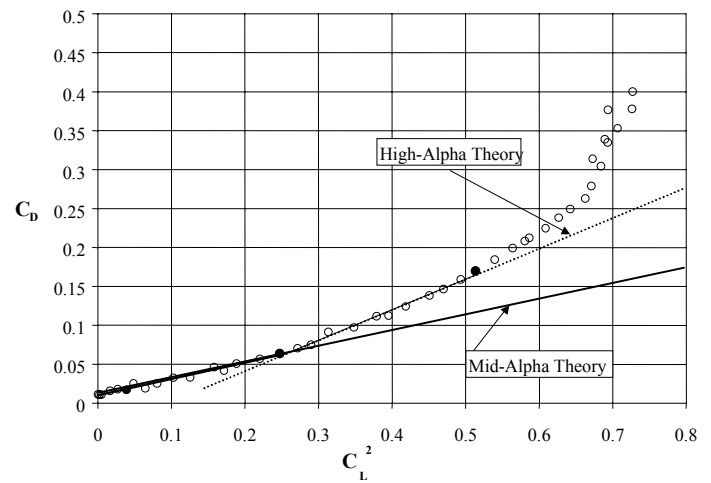
between the vortices. Force and moment data analysis showed distinct flow states depending on UCAV angle-of-attack. CFD was found to predict the gross flowfield features well, but had difficulty in predicting the pressure dynamic frequency content. CFD force and moment predictions was adequate. Future directions for vehicle control will be focused on wing vortex manipulation through the use of micro-vortex generators or fences.

REFERENCES

1. Kulfan, R.M., "Wing Airfoil Shape Effects on the Development of Leading Edge Vortices," AIAA Paper 79 1675, Reno, NV, January 1979.
2. Billman, G.M., Osborne, B.A., "High L/D Extended Range/Payload Fighter Aircraft Technology," AFRL VA-WP-TR-1999-3084, November 1998.
3. Washburn, A.E., Jenkins, L.N., and Ferman, M.A., "Experimental Investigation of Vortex-Fin Interaction," AIAA 31st Aerospace Sciences Meeting and Exhibit, AIAA 93-0050, Reno, NV, January 1993.
4. Bendat, J.S., and Piersol, A.G., *Engineering Applications of Correlation and Spectral Analysis*, Wiley Publishing, 1980.
5. Welch, P.D., "The Use of Fast Fourier Transform for the Estimation of Power Spectra: A Method Based on Time Averaging Over Short, Modified Periodograms," *IEEE Trans. Audio Electroacoust.*, Vol. AU-15, June 1967.
6. Strang, W.Z., "Parallel Cobalt User's Manual," AFRL, CFD Research Branch Report, Wright-Patterson AFB, OH, September 1999.
7. Strang, William Z., Tomaro, Robert F., Grismer, Matthew J., "The Defining Methods of Cobalt₆₀: A Parallel, Implicit, Unstructured Euler/Navier-Stokes Flow Solver," AIAA Paper 99-0786, January 1999.
8. Rae, W.H., Pope, A. Low-Speed Wind Tunnel Testing, 2nd Edition, Wiley, New York, 1984.
9. Polhamus, E.C., "A Concept of the Vortex Lift of Sharp-Edge Delta Wings Based on a Leading-Edge Suction Analogy," NASA TN D-3767, December 1966.
10. Chu, J., Luckring, J.M., "Experiemental Surface Pressure Data obtained on a 65° Delta Wing Across Reynolds Number and Mach Number Ranges Volume 2 – Small-Radius Leading Edge." NASA TM 4645, February 1996.

Table 2 - Maximum Strouhal Number						
α	Transducer 8	Transducer 9	Transducer 10	Transducer 11	Transducer 12	Transducer 13
12	10.1567	10.1348		7.0207		
13	8.7247	10.3698	9.0184	8.7247	5.8456	
14	7.0795	10.1348	8.6071	11.0161		
15	6.5507	8.7834	7.9608	10.5461		
16	8.1371	7.4908		8.6071	1.909	5.023
17	8.1959	8.2546		9.5472	1.909	4.9643
18					1.7915	3.3191

Table 3 - CFD comparison with experiment for mean and standard deviation of pressure coefficient											
					Cp Mean						
Transducer	1	2	3	5	6	7	8	9	10	12	13
Experiment	-0.2804	-0.528	-0.4712	-1.5909	0.4118	-2.0539	-2.9637	-1.4218	-2.4665	-1.0385	-0.4711
CFD	-0.0696	NA	-0.2881	-0.7308	0.4036	-1.0255	-1.4158	NA	-1.6323	-0.1762	-0.5220
					Cp Standard Deviation						
Transducer	1	2	3	5	6	7	8	9	10	12	13
Experiment	0.0181	0.0211	0.0188	0.0394	0.0107	0.0372	0.0959	0.0958	0.0875	0.1343	0.0213
CFD	0.0044	NA	0.0102	0.0154	0.0138	0.0112	0.0095	NA	0.0276	0.0047	0.0047

Fig. 7 – C_L vs. α Fig. 8 – C_D vs. C_L^2

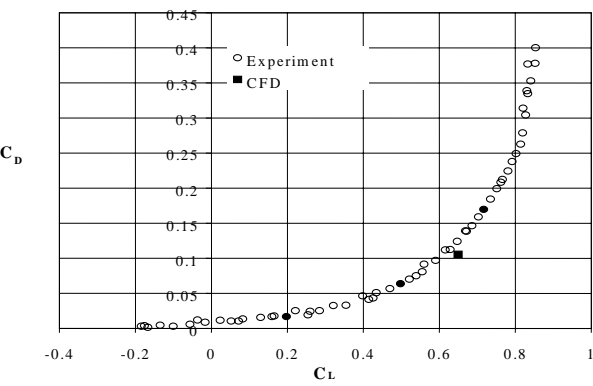


Fig. 9 – C_D vs. C_L

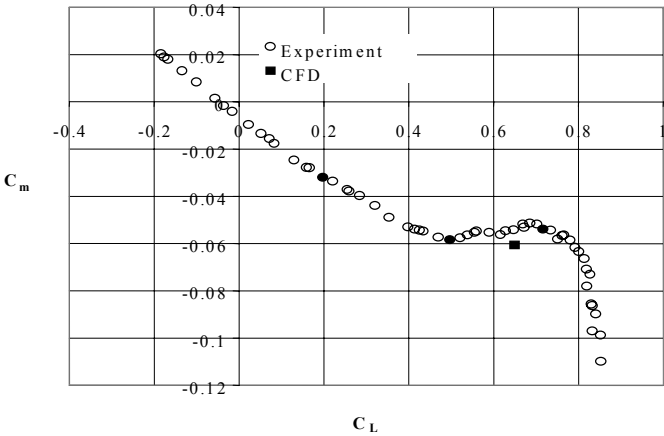


Fig. 10 – C_m vs. C_L

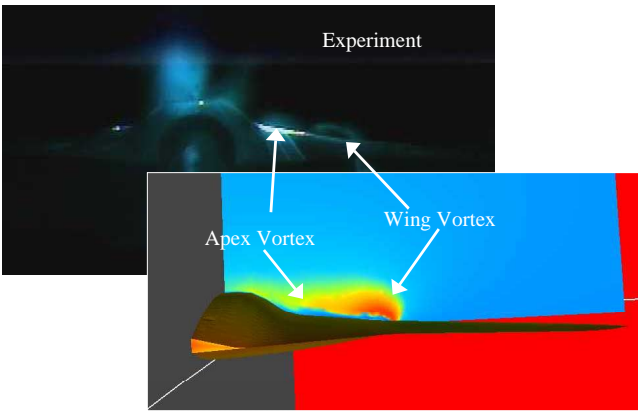


Fig. 11 - CFD Flow Visualization

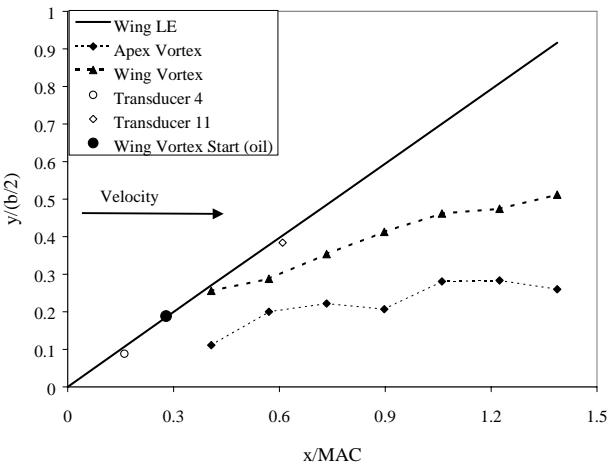


Fig. 12 – Vortex Location Found From Flow Visualization, $\alpha = 10$ Degrees

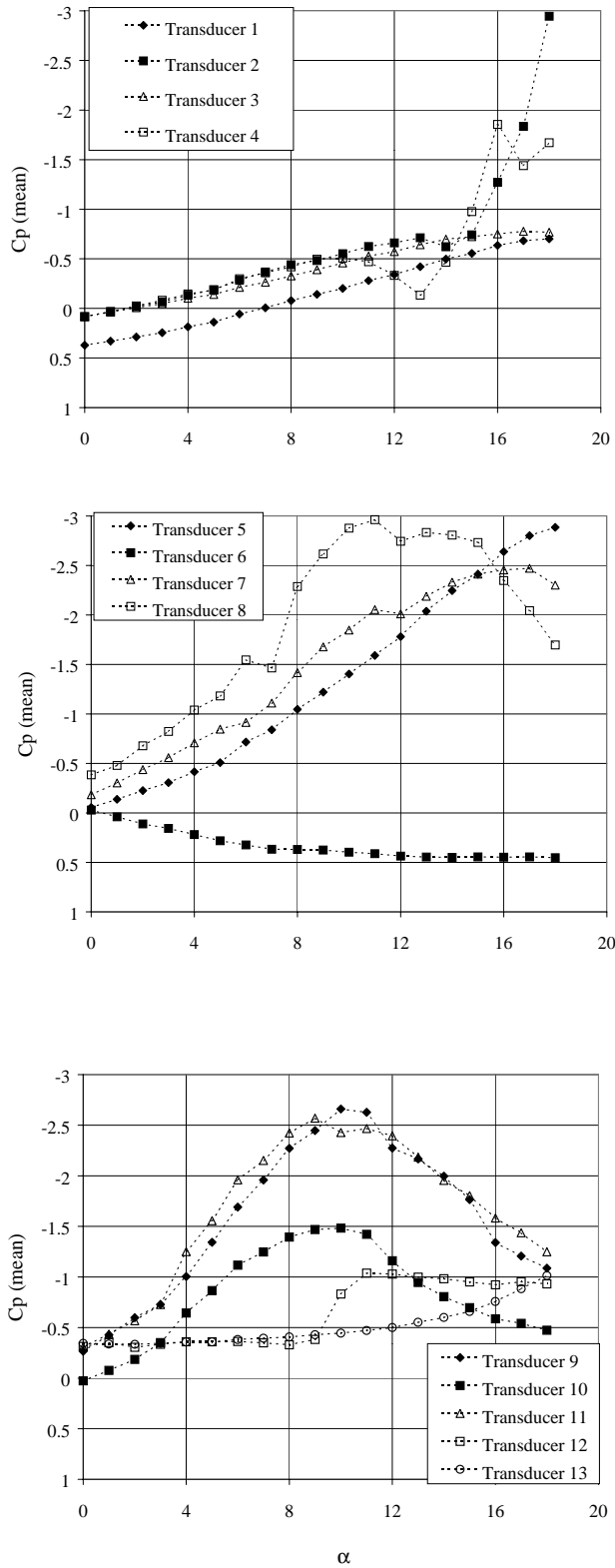


Fig. 13 – Mean Pressure vs. Angle-of-Attack, Unsteady Pressure Data

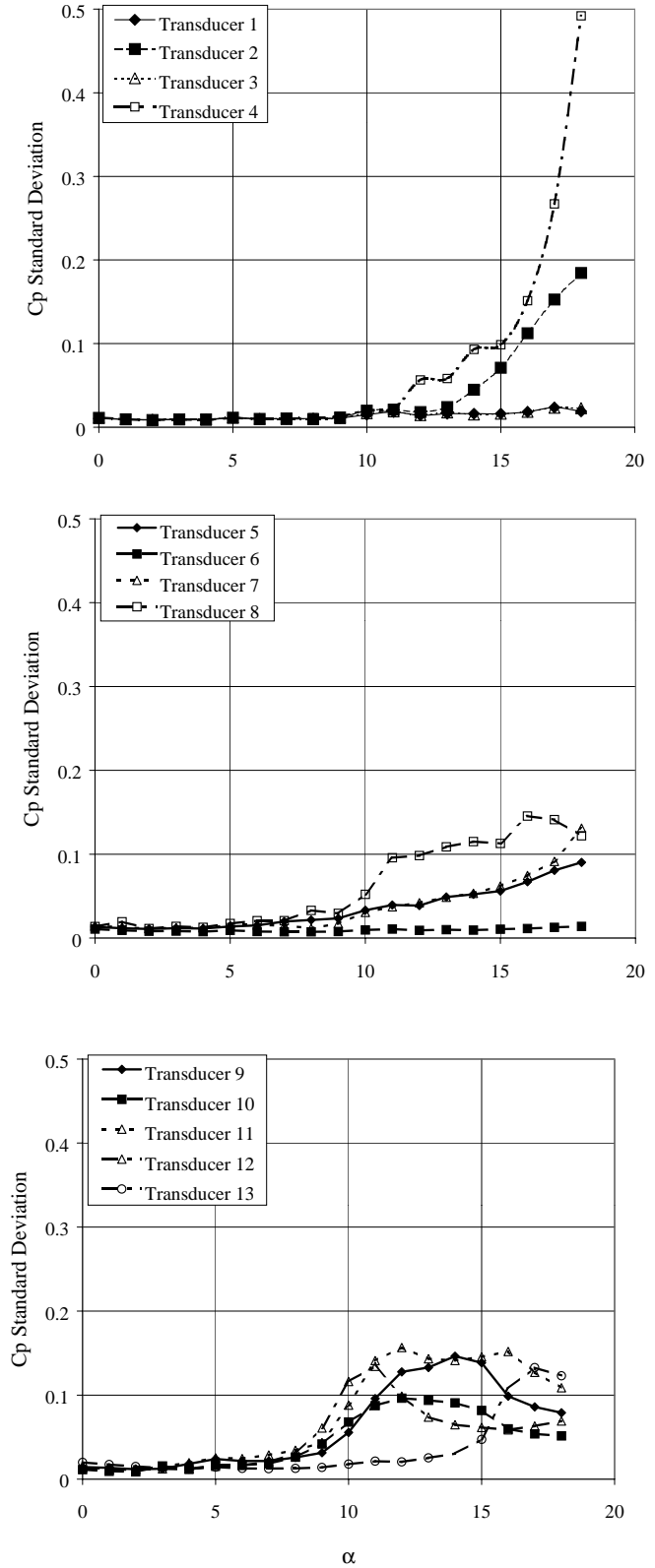


Fig. 14 – Standard Deviation vs. Angle-of-Attack, Unsteady Pressure Data

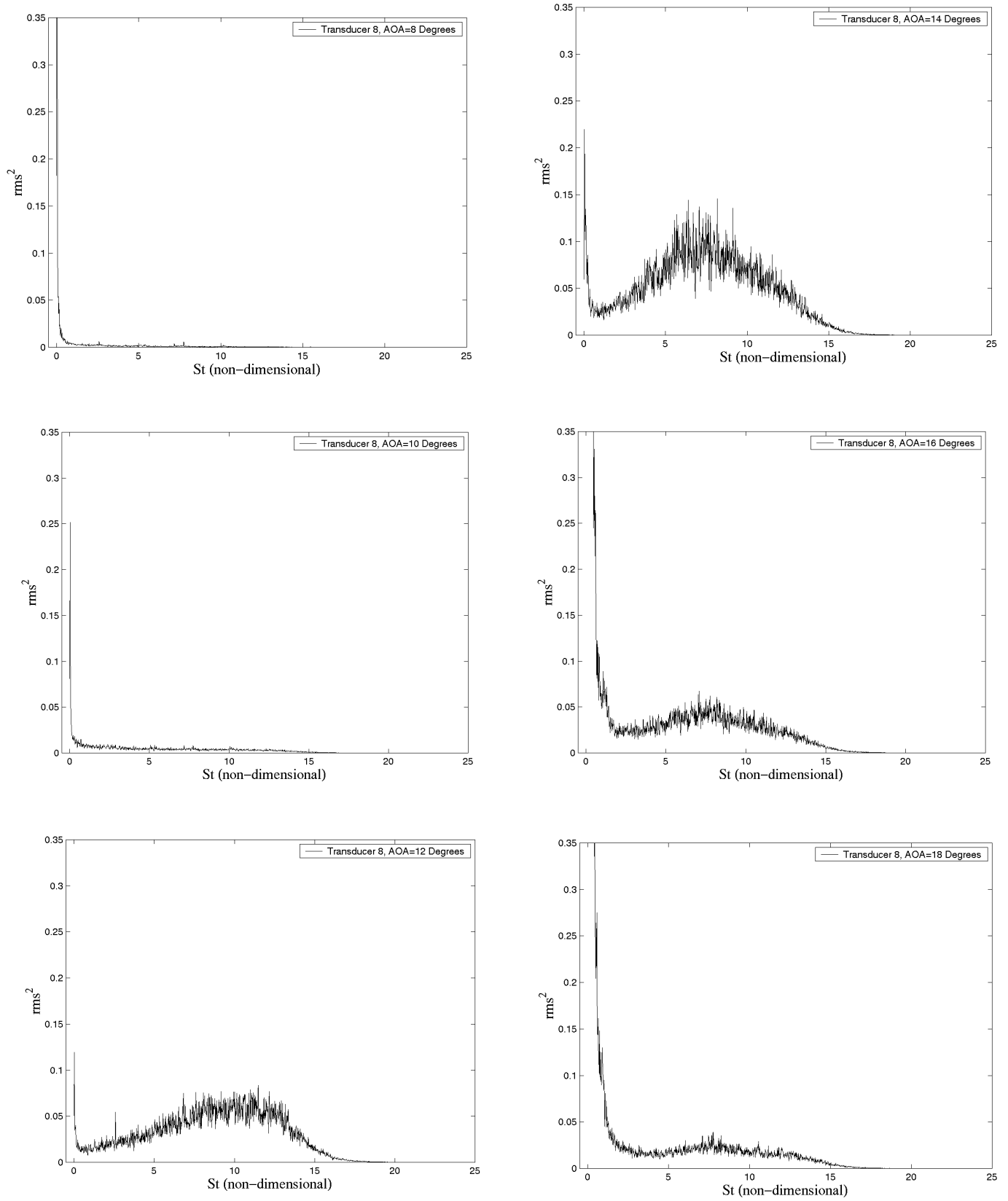


Fig. 15 – PSD For Transducer 8, Increasing Angle-of-Attack

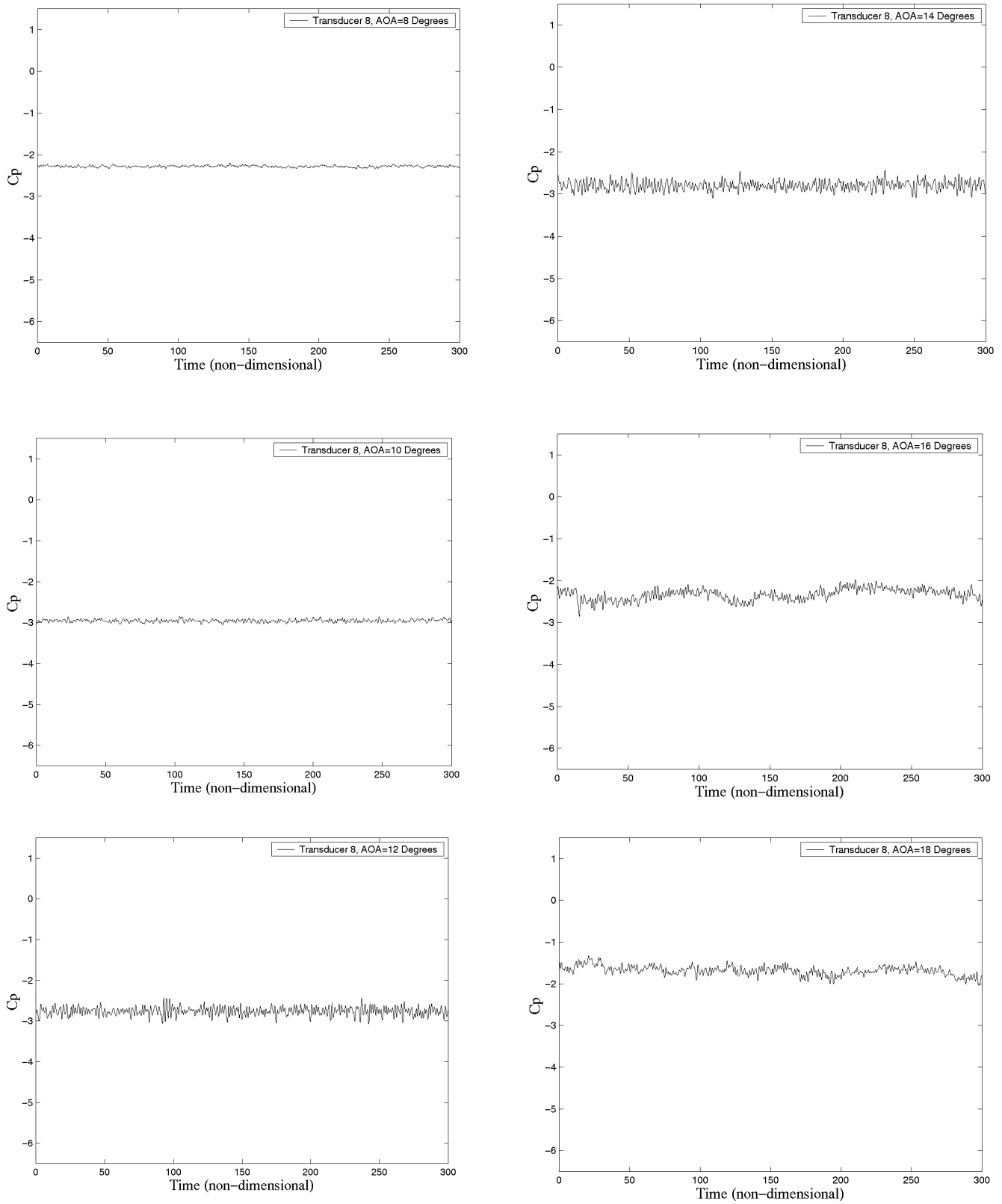


Fig. 16 – Time History For Transducer 8, Increasing Angle-of-Attack

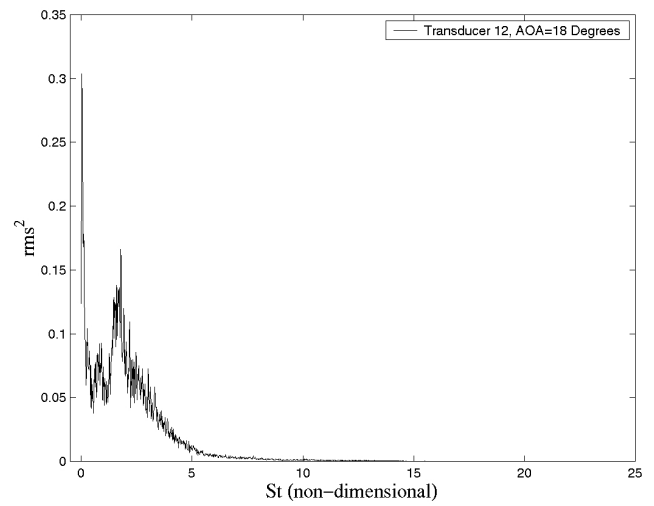
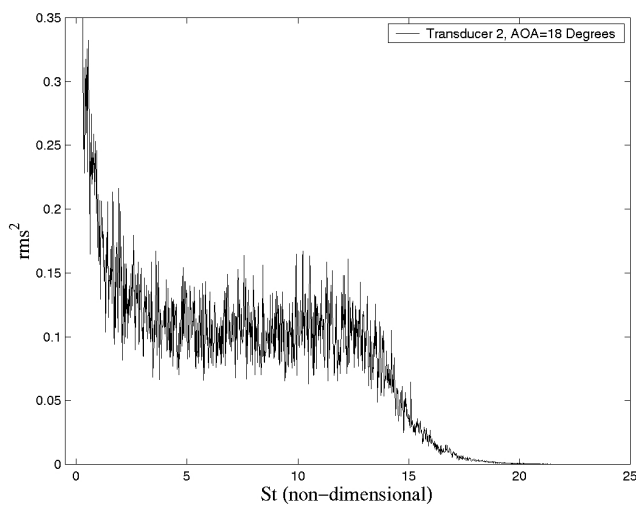
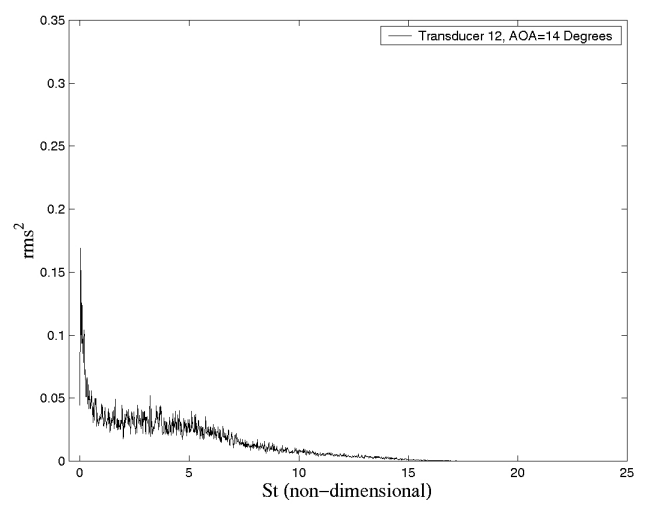
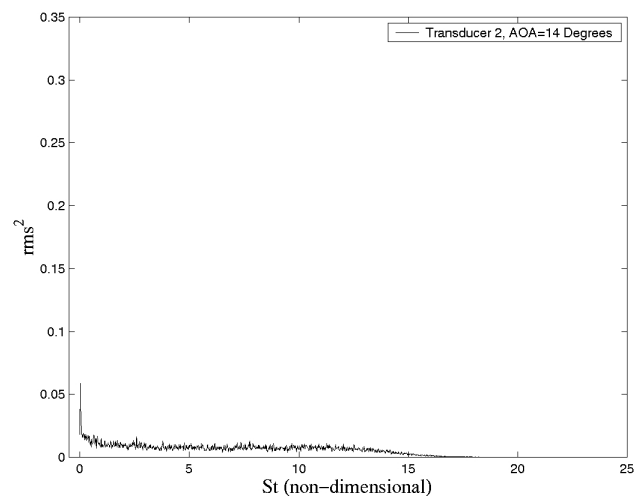
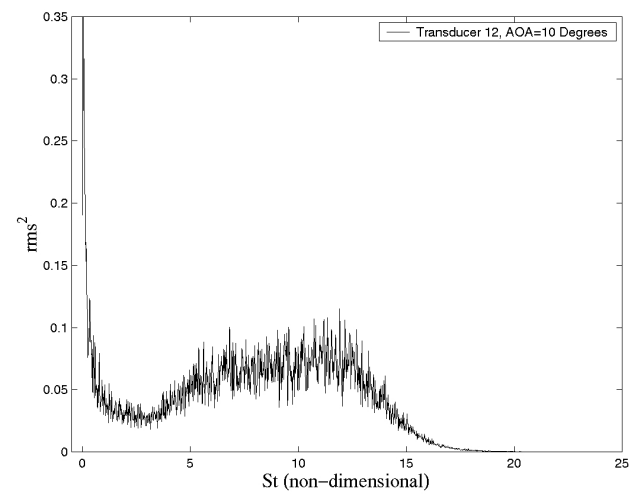
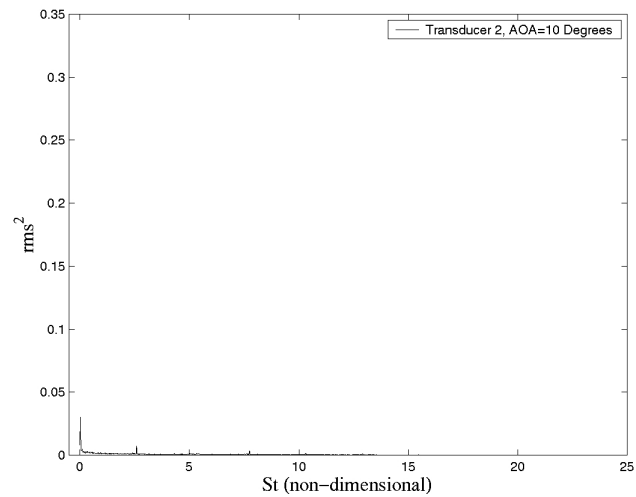


Fig. 17 – PSD for Transducer 2,
Increasing Angle-of-Attack

Fig. 18 – PSD for Transducer 12,
Increasing Angle-of-Attack

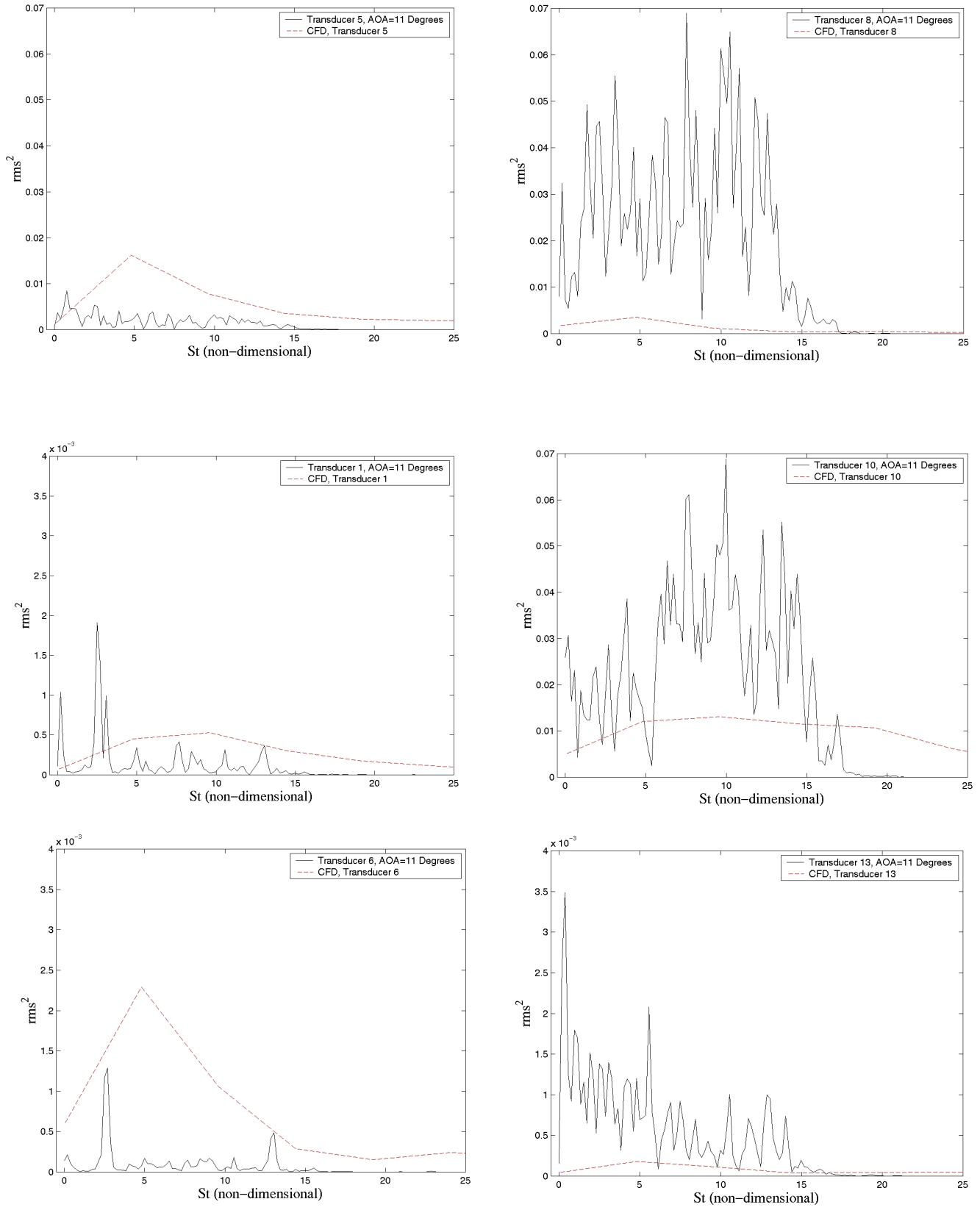


Fig. 19 – CFD Comparison to Selected Experimental Data, PSD

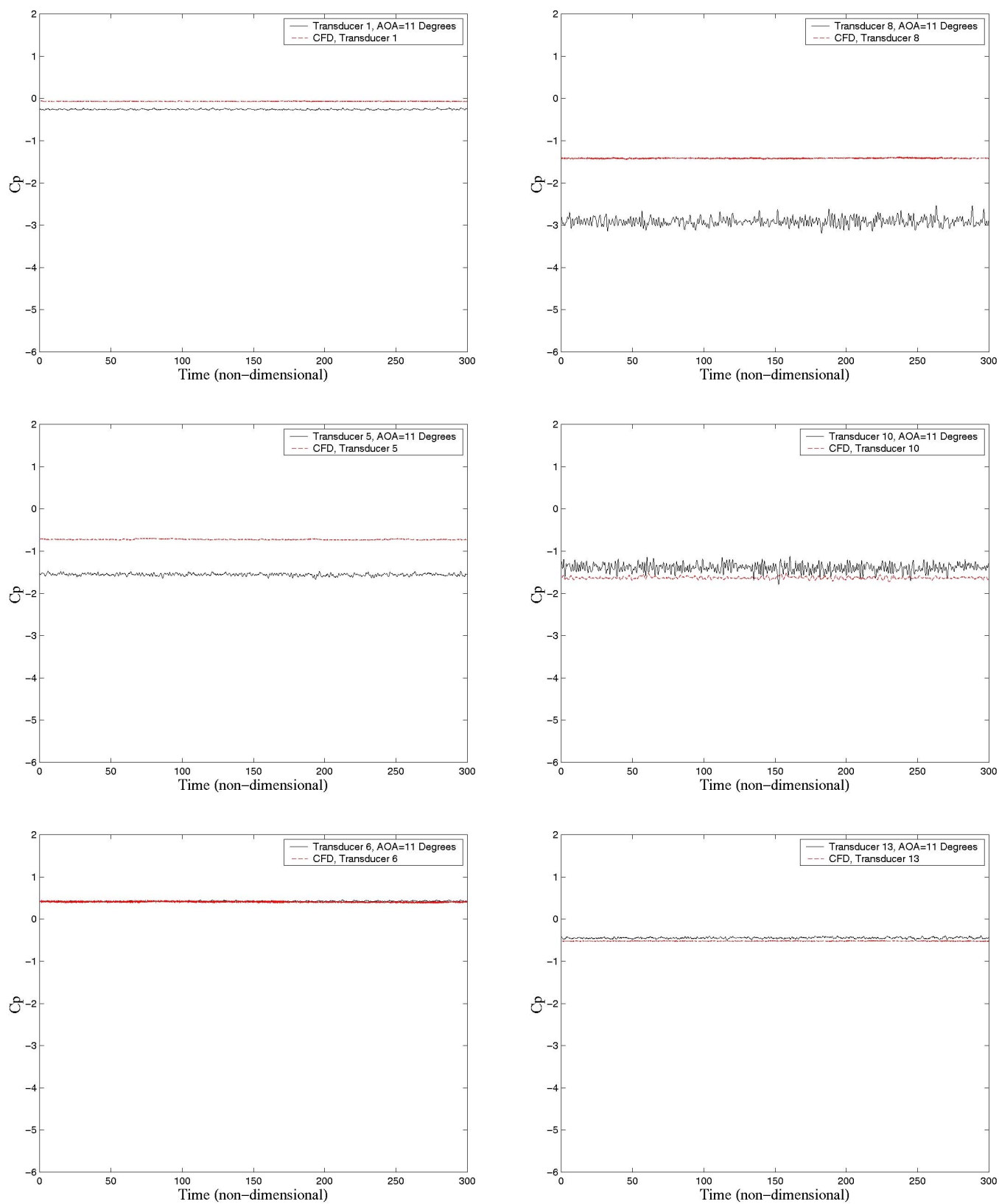


Fig. 20 – CFD Comparison to Selected Experimental Data, Time History

Paper: 34

Author: Mr. Ghee

Question by Dr. Khalid: You have carried out your experimental and CFD studies at Mach numbers and Reynolds numbers that are somewhat lower than that for which such UCAV configurations were designed. Would it be easy for you to incorporate the scale effects, or would you have to repeat such investigations at more appropriate flow conditions?

Answer: If appreciable vortex flow control is achieved at what you correctly state, an unrealistic Reynolds Number, the next step would be to test at realistic flight or near flight Reynolds numbers. Low speed, $M=0.45$, data from the Boeing polysonic wind tunnel, agree well. However, transonic Mach numbers could be quite different.

This page has been deliberately left blank



Page intentionnellement blanche